MODELING AND DIGITAL CONTROL OF AN ACTIVE MAGNETIC BEARING SYSTEM

CHIP RINALDI SABIRIN[1], ANDREAS BINDER[1],
DUMITRU DANIEL POPA[2], AURELIAN CRĂCIUNESCU[2]

Key words: Active magnetic bearings, Mathematical model, PID controller, State-Space method.

Active Magnetic Bearings (AMB) support a body by magnetic pulling forces, without any mechanical contact. The main advantages of such bearings compared with the traditional solutions are: absence of mechanical friction and wear, lubricant-free operation and therefore suitability for severe environments and applications, active vibration control and unbalance compensation. This paper deals with modeling, simulation and control of radial active magnetic bearing system for a high-speed drive. The system model from previous works [1, 5] has been extended with a model of the power amplifier with PWM control. Hence, dynamic behavior of currents in the bearing windings can also be investigated with this model. Two different controllers are used in the work, *i.e*. PID and state-space controller. Both will be compared to each other for two cases: a) lift-off of the rotor, and b) unbalance in the rotor which causes periodical disturbance force, which has also to be compensated by the magnetic bearing, additionally to the gravitation force.

1. **INTRODUCTION**

Magnetic bearings have been a research topic for several decades. During this time, magnetic bearings have evolved into an industry product that – due to its advantages over conventional bearing technology – is used in many practical applications as: turbo molecular vacuum pumps, gas pipeline centrifugal compressors, sealed pumps, and electric utilities power plant equipment. This progress was possible due to progress made in power electronics, microprocessors and digital control.

Today, there are two trends in AMB technology: on the one hand the *high speed* drives gain more importance especially in the machining and vacuum technology, and on the other hand, analog control is abandoned in favor of *digital*

[1] Technische Universität Darmstadt, Institut fur Elektrische Energiewandlung, Landgraf-Georg-Str. 4, Darmstadt, E-mail: abinder@ew.tu-darmstadt.de.
[2] "Politehnica" University of Bucharest, Electrical Engineering Department 313 Splaiul Independentei, Bucharest, E-mail: ac_drive@temp.eltech.pub.ro.

Rev. Roum. Sci. Techn. – Électrotechn. et Énerg., **52**, *2,* p. 157–181, Bucarest, 2007

control, which offers much more flexibility for taking full advantage of the AMB technology. For the operation of the AMB system, position control is necessary, since the magnetic force system is inherently unstable. The design of such control is a challenging task since it must compensate for the instability inherent to the magnetic bearing and at the same time avoid destabilization of any flexible modes the rotor may exhibit, especially at high speed, which is aimed in our case at 40 000 min^{-1} and for a rotor with a mass of 14 kg. At the moment this high speed drive is supported by AMB with analogue control [8], which shall be replaced by digital control in the future.

The purpose of this paper is to contribute to digital controller design for AMB rotor system. This paper follows two directions:

1. *Identification of AMB rotor system model*, with detailed modeling of PWM of current controller.

2. *Digital controller design*, searching for a well-suited controller that fits for all necessities. Two types of controllers were distinguished and will be discussed:

a) *PID* controllers and b) State-space controllers based on *LQR method* (*Linear Quadratic Regulator*).

Since in large-signal model the unstable AMB is non-linear, the most useful approaches are: (i) to use differential windings magnetic bearing to reduce the influence of non-linearity and (ii) to linearize the model in a small region around equilibrium points in order to use linear control techniques. However, the performance of a single operating point linear controller can be quite good only near the equilibrium conditions. As the variation of the rotor position is small due to the small air gap of AC motors, this method of linearization applies well.

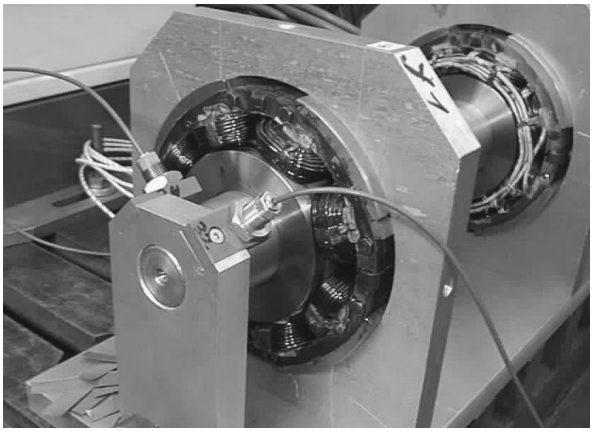

Fig. 1 – Magnetic bearing demonstrator with two radial bearings (max. force 230 N).

Comparisons between PID and state-space controller for magnetic bearings are available in several publications in the past, for example [6] and [7]. For a current research on high-speed machine with 40 000 min^{-1} at *Technische Universität Darmstadt*, the comparison here shall be done with a demonstrator (Fig. 1), so previous simulation of the control software is necessary, which is included here.

2. **MODELS AND FORMULATIONS**

The core of AMB system is an electromagnet, which creates a magnetic field that provides a magnetic pull force that supports the body without mechanical contact, if a current is passed through electromagnet coil. The AMB exerts an attractive force on the body that opposes the gravitational force, which pulls the body downward. If the current is kept constant, and the body is moving downward, the magnetic force on the body is decreasing as the distance between electromagnet and body is increasing. This leads to the body falling down. If the body is moving upwards, the attractive magnetic force is increasing, and the body is accelerated towards the electromagnet.

To avoid this unstable behavior, the electric current must be permanently adjusted. A position sensor (*e.g.* capacitive or eddy-current sensor) measures the deviation from reference position. Based on this measurement a control system (controller/microprocessor) computes the value of current that must be applied to electromagnet coil and sends this information to power amplifier. The power amplifier generates this electric current, which excites the electromagnet coil. With an appropriately designed controller the body can be held at its reference position, and system dynamics can be adjusted in a wide range.

In technical applications, *differential winding bearings* are used. So, for positioning the rotor in one axis, a second magnet identical to first one, but exerting pulling force in opposite direction, is used. The non-linear force-distance characteristic tends to be more linear. It improves the dynamics, since now the forces on the rotor body can be exerted in both directions of axes. The AMB system (Fig. 2) has two degrees of freedom. The two opposing electromagnets are operating in *differential winding mode* (Fig. 3). A constant *bias current* i_0 is exciting basic excitation coils for generating the magnetic field, and the *control current* i_c is exciting an additional control field which exerts pull forces in positive direction, so adding to the field of one magnet, and subtracting to the opposite magnet.

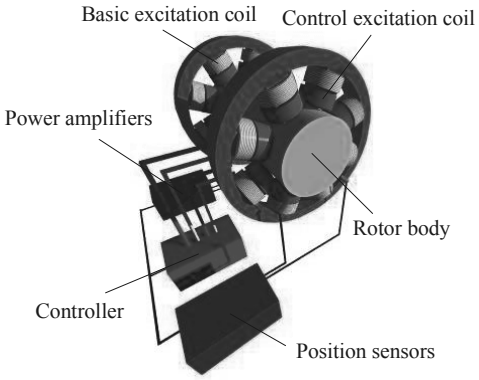

Fig. 2 – AMB system model.

A. *Magnetic force model*

In order to obtain the equation that is describing the AMB behavior the following assumptions are used:

– The permeability of iron part is infinitely high (= ideally unsaturated iron).

– The magnetic flux density B is homogeneously distributed in the iron core and the air gap.

– The magnetic pole cross-sectional areas are constant along the magnetic circuit.

In air gap, flux density B is proportional to magnetic field strength H, so the radial force can be expressed as a function of coil current i and air gap d.

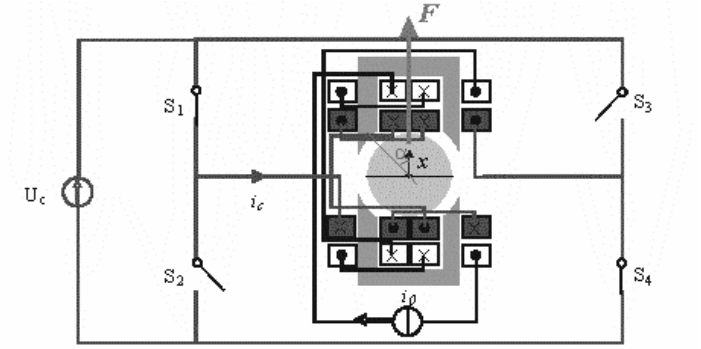

Fig. 3 – Magnetic bearing with differential windings, connected at constant bias current i_o and switched power amplifier injecting the control current i_c .

With control and bias current i_c, i_0 and $x = (d_0 - d)\cdot\cos\alpha$, where i_0, d_0 are current and air gap, when rotor is placed in symmetric axis and α is the angle under which the magnetic force attracts the rotor [2], equation (1) is obtained:

$$F = k \cdot \left[\frac{(i_0 + i_c)^2}{(d_0 - x)^2} - \frac{(i_0 - i_c)^2}{(d_0 + x)^2} \right] \cdot \cos\alpha; \tag{1a}$$

$$k = \mu_0 \cdot N^2 \cdot A/4; \tag{1b}$$

with $\mu_0 = 4\pi 10^{-7}$ H/m stands for the vacuum magnetic permeability, N is coil number of turns and A is iron cross-sectional area. Equation (1b) is valid, if number of turns of basic and control coils N_0 and N_c are identical: $N_0 = N_c = N$, otherwise $i_0' = (N_0/N_c) \cdot i_0$ has to be used.

Table 1

Simulation: AMB parameters

Maximum force F_{max}	230	N
Rotor mass, m	14	kg
Air gap, d	0.6	mm
Bias current, i_0	6	A
Control current, i_c	15	A
No. of turns for basic excitation N_0	46	
No. of turns for control excitation N_c	18	

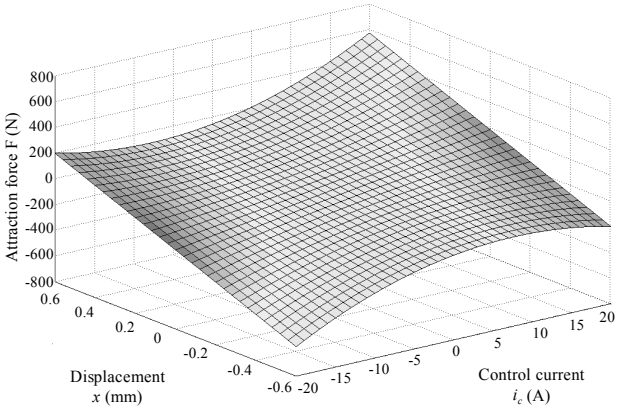

Fig. 4 – Calculated attraction force $F(i_c, x)$ of differential winding mode, showing more linear behaviour (one radial bearing of the demonstrator Fig. 1).

Equation (1a) and Fig. 4 show the quadratic dependence of force with *control current* i_c and inversely quadratic dependence with *air gap d*, which – due to differential winding mode – gives a wide range of linear dynamic operation as equation (2)

$$F \approx k_i \cdot i_c + k_x \cdot x \,. \tag{2}$$

B. *Rigid body rotor model*

The mathematical model does not take into account axial movement, this being justified by negligible coupling effect between the radial and axial dynamics [2]. So, the mathematical model refers only to a rigid rotor body, suspended in two identical radial active magnetic bearings.

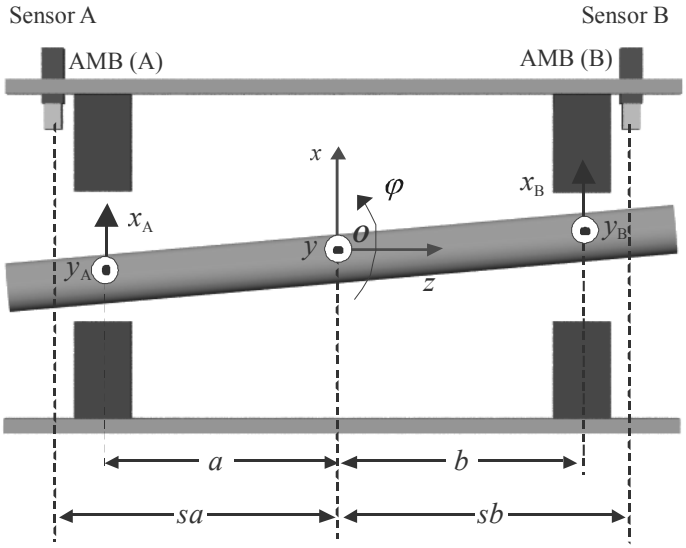

Fig. 5 – Magnetically suspended rigid rotor shaft.

The rotor dynamics in the *x*-*z*-plane can be described using displacement *x* of rotor's center of gravity *O* and rotation angle φ between rotor and horizontal *z*-axis through O (Fig. 5). Usually, even for high-speed operation rotational speed *n* of rotor is kept well below 70 % of first bending natural frequency f_e, so the rotor may be treated as rigid body. The rather low dynamic elasticity of AMB due to the low value of k_x gives vibration of the rigid body in the bearings, called common mode and differential mode vibration. From Fig. 5 with force and torque in *x*-*z*-plane and

y-*z*-plane, the mechanical equation for evaluating the AMB system dynamic behavior, considering rotating rigid rotor vibration, can be written as:

$$\boldsymbol{f} = \boldsymbol{M} \cdot \ddot{\boldsymbol{z}} + \boldsymbol{G} \cdot \dot{\boldsymbol{z}} . \tag{3}$$

In (3), $\boldsymbol{f} = \begin{pmatrix} f_{\mathrm{x}} & p_{\mathrm{y}} & f_{\mathrm{y}} & -p_{\mathrm{x}} \end{pmatrix}^{\mathrm{T}}$ is *force and torque component vector* [2], $\boldsymbol{M}$ is *mass matrix* (see Equation (6)), $\boldsymbol{G}$ is *gyroscopic matrix* (see Equation (7)) and $\boldsymbol{z} = \begin{pmatrix} x & \beta & y & -\alpha \end{pmatrix}^{\mathrm{T}}$ is *coordinate component vector*, using the global coordinate system *x, y, z*. In order to give a proper command, (3) must be translated in AMB coordinate system using a *transformation matrix* $\boldsymbol{T}$, with the axial distance *a*, *b* of the radial bearings from O [2].

$$\boldsymbol{T} = \frac{1}{a+b} \cdot \begin{bmatrix} b & a & 0 & 0 \\ -1 & 1 & 0 & 0 \\ 0 & 0 & b & a \\ 0 & 0 & -1 & 1 \end{bmatrix}. \tag{4}$$

With $\boldsymbol{f}_{\mathrm{c}} = \boldsymbol{T} . \boldsymbol{f}$, $\boldsymbol{z}_{\mathrm{c}} = \boldsymbol{T} . \boldsymbol{z}$, we get:

$$\boldsymbol{f}_{\mathrm{c}} = \boldsymbol{M}_{\mathrm{c}} \cdot \ddot{\boldsymbol{z}}_{\mathrm{c}} + \boldsymbol{G}_{\mathrm{c}} \cdot \dot{\boldsymbol{z}}_{\mathrm{c}}. \tag{5}$$

In (5) the subscript *c* denotes the control coordinate system. $\boldsymbol{M}_{\boldsymbol{c}}$, $\boldsymbol{G}_{\boldsymbol{c}}$ and $\boldsymbol{z}_{\boldsymbol{c}}$ have following expressions, where *m* is rotor mass, I_{x}, I_{y}, I_{z} are rotor inertia moments around *x, y, z*-axis and $\Omega = 2\pi n$ is angular speed around *z*-axis. With the use of inverse $\boldsymbol{T}'$ of matrix $\boldsymbol{T}$ we get:

$$\boldsymbol{M}_{\boldsymbol{c}} = \boldsymbol{T}' \cdot \boldsymbol{M} \cdot \boldsymbol{T} = \boldsymbol{T}' \cdot \begin{bmatrix} m & 0 & 0 & 0 \\ 0 & I_{\mathrm{x}} & 0 & 0 \\ 0 & 0 & m & 0 \\ 0 & 0 & 0 & I_{\mathrm{y}} \end{bmatrix} \cdot \boldsymbol{T}, \tag{6}$$

$$\boldsymbol{G}_{\boldsymbol{c}} = \boldsymbol{T}' \cdot \boldsymbol{G} \cdot \boldsymbol{T} = \boldsymbol{T}' \cdot \left(\begin{bmatrix} 0 & 0 & 0 & 0 \\ 0 & 0 & 0 & 1 \\ 0 & 0 & 0 & 0 \\ 0 & -1 & 0 & 0 \end{bmatrix} \cdot I_{\mathrm{z}} \cdot \Omega \right) \cdot \boldsymbol{T}, \tag{7}$$

$$\boldsymbol{z}_{\boldsymbol{c}} = \begin{bmatrix} x_{\mathrm{A}} \\ x_{\mathrm{B}} \\ y_{\mathrm{A}} \\ y_{\mathrm{B}} \end{bmatrix}. \tag{8}$$

Equation (2) describes a scalar equation, which is valid for Fig. 3. For describing Fig. 5, it will be written as vector equation

$$\boldsymbol{f}_{\mathrm{c}} = \boldsymbol{K}_{\mathrm{x}} \cdot \boldsymbol{z}_{\mathrm{c}} + \boldsymbol{K}_{\mathrm{i}} \cdot \boldsymbol{i}_{\mathrm{c}} \,. \tag{9}$$

Force-displacement factors matrix $\boldsymbol{K}_{\mathrm{x}}$ and *force-current factors matrix* $\boldsymbol{K}_{\mathrm{i}}$ represent the elements that link the mechanical equations with electric ones for *x*- and *y*-direction of bearings (A) and (B). The variable $\boldsymbol{i}_{\mathrm{c}}$ represents the control current vector $\boldsymbol{i}_{\boldsymbol{c}} = \begin{pmatrix} i_{x\mathrm{A}} & i_{x\mathrm{B}} & i_{y\mathrm{A}} & i_{y\mathrm{B}} \end{pmatrix}^{\mathrm{T}}$.

$$\boldsymbol{K}_{\mathrm{x}} = \begin{bmatrix} k_{\mathrm{x}\_x\mathrm{A}} & 0 & 0 & 0 \\ 0 & k_{\mathrm{x}\_x\mathrm{B}} & 0 & 0 \\ 0 & 0 & k_{\mathrm{x}\_y\mathrm{A}} & 0 \\ 0 & 0 & 0 & k_{\mathrm{x}\_y\mathrm{B}} \end{bmatrix};$$

$$\boldsymbol{K}_{\mathrm{i}} = \begin{bmatrix} k_{\mathrm{i}\_x\mathrm{A}} & 0 & 0 & 0 \\ 0 & k_{\mathrm{i}\_x\mathrm{B}} & 0 & 0 \\ 0 & 0 & k_{\mathrm{i}\_y\mathrm{A}} & 0 \\ 0 & 0 & 0 & k_{\mathrm{i}\_y\mathrm{B}} \end{bmatrix}. \tag{10}$$

Considering gravitation and disturbance force vectors $\boldsymbol{f}_{\mathrm{g}}$ and $\boldsymbol{f}_{\mathrm{d}}$, equation (5) will be extended to

$$\boldsymbol{f}_{\mathrm{c}} + \boldsymbol{f}_{\mathrm{g}} + \boldsymbol{f}_{\mathrm{d}} = \boldsymbol{M}_{\mathrm{c}} \cdot \ddot{\boldsymbol{z}}_{\mathrm{c}} + \boldsymbol{G}_{\mathrm{c}} \cdot \dot{\boldsymbol{z}}_{\mathrm{c}}. \tag{11}$$

Based on (9), (10) and (11), Fig. 6 shows the AMB model.

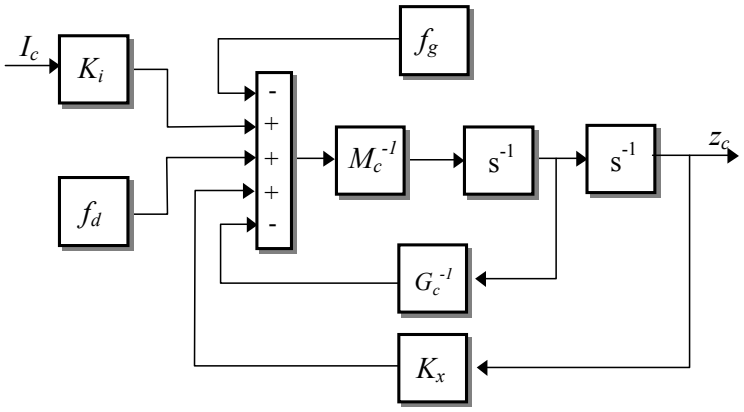

Fig. 6 – AMB system model.

C. *PWM inverter model*

One of the extensions to the previous works, [1] and [5], is the modeling of power amplifiers. Four switch mode MOSFET full-bridges inject control current i_c into the bearing windings with a switching frequency of 50 kHz. The bearing windings are modeled by the transfer function $\frac{I(s)}{U(s)} = \frac{1}{(sL+R)}$ with a current slope of maximum 50 A/ms due to the inductivity of 500 μH and resistance of 500 mΩ of the windings.

Given a reference current by the position controller, the current controller calculates appropriate duty cycles for the MOSFETs of the full-bridges. As a two-level PWM hardware, the full-bridges apply either +24V or –24V on the bearings windings, with a duration depending on the mentioned duty cycle. The simulated current behavior of the PWM inverter model is depicted in Fig. 7. The current ripple shows conformity to real current behavior of the power amplifiers.

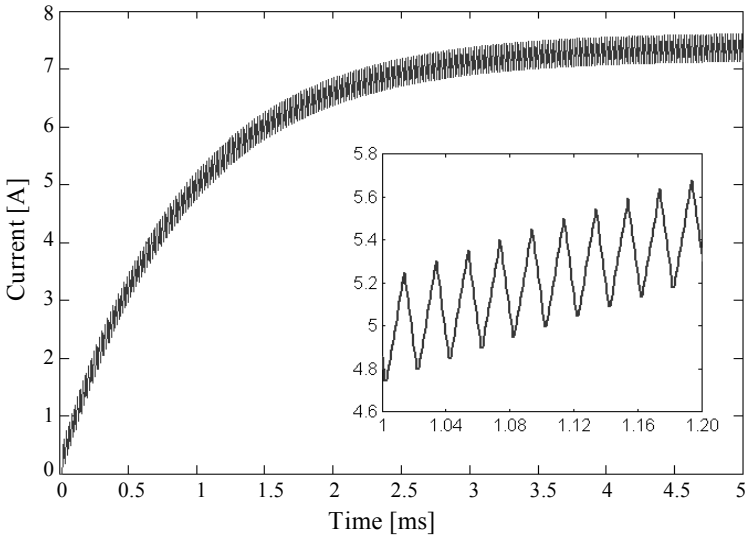

Fig. 7 – Calculated control current of the PWM inverter model for *y*-axis of radial bearing with 7.5 A set-point value.

3. **CONTROL SYSTEM**

Extending previous works in [1] and [5], following improvements are done:

1. Design of PID controller in digital method.

2. Design of decentralized state-space controller for each bearing axis with reduced observer. Simulation is performed in fixed-step calculations.

3. Modeling of power amplifier injecting control current i_c into bearing windings.

Based on the AMB model for both radial bearings (A) and (B), two control methods are presented.

A. *PID control*

PID control method was already used at the early days of AMB [2]. It requires a small computing power and provides good robustness and stability, if the operating point is inside of linear performance range of the AMB. PID control procedure associated with design of decentralized controllers is able to control AMB systems with collocation of force direction and sensed direction of rotor movement at the position sensor's location, and gives stability for discrete time control.

For position control loop, we consider the AMB as Single Input Single Output (SISO) system. Hence, it is sufficient to investigate only one bearing axis, and we gain a transfer function of the AMB in z-domain of z-transform, using sampling time t_s:

$$\mathrm{H_P}(z) = \frac{b_1 \cdot z + b_0}{z^2 + a_1 \cdot z + a_0}, \tag{12}$$

with: $a = \frac{k_x}{m}$; $a_0 = 1$; $a_1 = -\mathrm{e}^{-\sqrt{a}\cdot t_s} - \mathrm{e}^{\sqrt{a}\cdot t_s}$; $b_0 = b_1 = \frac{k_\mathrm{i}}{2 \cdot \sqrt{k_x \cdot m}} \cdot \left(\mathrm{e}^{\sqrt{a}\cdot t_s} - \mathrm{e}^{-\sqrt{a}\cdot t_s}\right)$

As the closed loop transfer function is described as a fourth order system, for PID controller implementation an extended parallel model with four parameters K_P, K_I, K_D, r was chosen.

$$\mathrm{H_R}(z) = K_\mathrm{P} + \frac{K_\mathrm{I} \cdot z}{z-1} + K_\mathrm{D} \cdot \frac{z-1}{z-r}. \tag{13}$$

In (13) K_P is proportional gain, K_I is integrative gain, K_D is derivative gain and the fourth parameter r is the coefficient of derivative filter, used in order to limit step variations of derivative term as a consequence of fast changes.

To assure a good system response at set-point reference variations even at high frequencies, a feed-forward controller is added into the controller model. In this case the feed-forward controller transfer function is the inverse of discrete plant transfer function in z-domain (12).

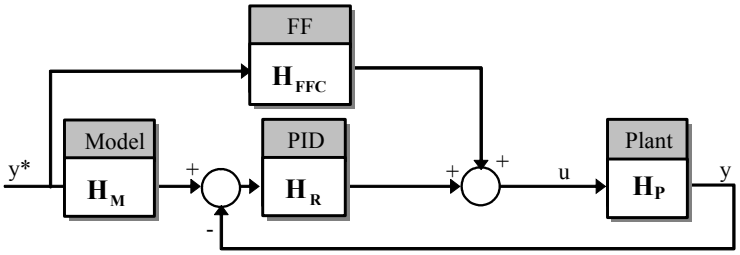

Fig. 8 – AMB control structure with PID controller.

Table 2

PID controller parameters

Proportional gain, K_P	1.5
Integrative gain, K_I	0.0025
Saturation limit for integrative part, I_{LIM}	300 bits
Time after that the integration is started, I_{TIME}	1 ms
Derivative gain, K_D	10
Derivative filter gain, r	–0.0033
Sampling time, t_s	0.1 ms

In Fig. 8, H_R and H_P represent the controller respectively plant transfer function, H_{FFC} is the feed-forward controller transfer function and H_M is the reference model taken into consideration.

$$H_{FFC}(z) = \frac{b_1 \cdot z + b_0}{z^2 \cdot (b_1 + b_0)} \cdot \frac{1}{H_P(z)}. \tag{14}$$

The corresponding reference model is given by

$$H_M(z) = \frac{b_1 \cdot z + b_0}{z^2 \cdot (b_1 + b_0)}. \tag{15}$$

In Table 2, the PID main data obtained via polynomial method for poles allocation are presented.

B. *State-space control*

State-Space controller is perfectly suited for numerical computations. In the last years DSP (Digital Signal Processor) computation power has increased. A large variety of state space controllers can be implemented. The algorithm for controller parameters (K-vector as feed-back controller) is more complex than in PID controller's case. The method is based on matrices operations that describe the

system model, and for this reason, the inner state of the process can be accessed, not only inputs and outputs.

The first step, when dealing with a multivariable system design, is to perform the decoupling of MIMO (Multiple Input Multiple Output) system and to find an approximate model consisting of two or more SISO systems.

A continuous, linear, constant-coefficient system of differential equations can always be expressed as a set of first-order matrix differential equations [3]:

$$\mathbf{x}(k+1) = \Phi \ \ \mathbf{x}(k) + \Gamma \ \ \mathbf{u}(k); \tag{16a}$$

$$\mathbf{y}(k) = \mathbf{H} \ \ \mathbf{x}(k), \text{ with } \mathbf{H} = [1 \quad 0]; \tag{16b}$$

where $\boldsymbol{x}$ is the inner states vector, $\boldsymbol{u}$ is the control input vector and $\boldsymbol{y}$ represents the outputs vector and according to [4]

$$\mathbf{\Phi} = \mathrm{e}^{\mathbf{A}\cdot\mathrm{T}}; \ \mathbf{A} = \begin{bmatrix} 0 & 1 \\ \dfrac{k_{\mathrm{x}}}{m} & 0 \end{bmatrix}. \tag{17}$$

One of the most attractive features of state-space controller design method is that the procedure consists of two independent steps. First step assumes that all states are known. This assumption allows proceeding with first design step, namely, *control law*. Second step is to design an estimator, in order to estimate entire inner state vector. Finally, control algorithm will consist of a combination of control law and estimator, with control law calculations based on estimated state.

A control law that has considerable convenience is simply the feedback of linear combination of all state elements

$$\boldsymbol{u} = -\boldsymbol{K} \cdot \boldsymbol{x} = -[k_1 \quad k_2 \quad ...] \cdot [x_1 \quad x_2 \quad ...]^{\mathrm{T}}. \tag{18}$$

The control law design consists in finding elements of $\boldsymbol{K}$-vector, so that roots of *characteristic equation* (19) are in desired location.

$$\det \left| z \cdot \boldsymbol{I} - \mathbf{\Phi} + \mathbf{\Gamma} \cdot \boldsymbol{K} \right| = 0. \tag{19}$$

In this paper control $\boldsymbol{K}$-vector will be determined using LQR solution. The LQR solution may be found using two methods [4] :

1. First method is to compute $\boldsymbol{K}$-vector. From the beginning, in constant steps of the problem, the task is to compute $\boldsymbol{S}$ (solution of vector *Riccati* equation) backward in time until it reaches steady value S_∞ and then to use theory for *time varying optimal control*.

2. Second method is to look for steady-state solution of *Riccati* equation. In steady state $\boldsymbol{S}(k)$ becomes equal with $\boldsymbol{S}(k + 1)$ and in this case *algebraic Riccati equation* can be used. This method is going to be used for determining $\boldsymbol{K}$-vector.

As some of the states are directly measured, a reduced-order estimator will be used [4].

In order to pursue an estimator for unmeasured part, we partition the state vector $\boldsymbol{x}$ into two parts: $\boldsymbol{x}_a$ represent part directly measured (rotor position) or calculated respectively (rotor movement speed), and $\boldsymbol{x}_b$ is the remaining portion to be estimated (i.e. gravitation and disturbance force), as shown in (20).

$$\begin{bmatrix} \boldsymbol{x}_a(k+1) \\ \boldsymbol{x}_b(k+1) \end{bmatrix} = \begin{bmatrix} \boldsymbol{\Phi}_{aa} & \boldsymbol{\Phi}_{ab} \\ \boldsymbol{\Phi}_{ba} & \boldsymbol{\Phi}_{bb} \end{bmatrix} \cdot \begin{bmatrix} \boldsymbol{x}_a(k) \\ \boldsymbol{x}_b(k) \end{bmatrix} + \begin{bmatrix} \boldsymbol{\Gamma}_a \\ \boldsymbol{\Gamma}_b \end{bmatrix} \cdot \boldsymbol{u}(k), \tag{20a}$$

$$\boldsymbol{y}(k) = \begin{bmatrix} \boldsymbol{H}_a & \boldsymbol{H}_b \end{bmatrix} \cdot \begin{bmatrix} \boldsymbol{x}_a(k) \\ \boldsymbol{x}_b(k) \end{bmatrix}. \tag{20b}$$

Table 3

State space parameters

Control vector	$\boldsymbol{K}$ = [5.49 A/m ; 0.03 A/(m/s)]·10^4
Luenberger vector	$\boldsymbol{L}$ = [0.00006 N/m ; 1.39 N/(m/s)]·10^3

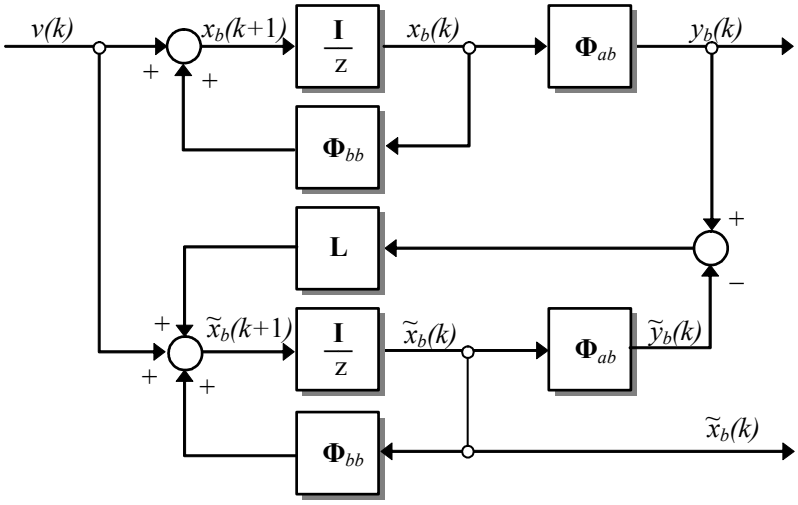

Fig. 9 – *Luenberger* observer block diagram.

From (20), we get the equations that describe unknown states vector part [4], as shown in (21).

$$x_b(k+1) = \mathbf{\Phi}_{bb} x_k(k) + \mathbf{y}_b(k), \tag{21a}$$

with:

$$y(k) = \mathbf{\Phi}_{ba} \mathbf{x}_a(k) + \mathbf{\Gamma}_b \mathbf{u}(k), \tag{21b}$$

$$\mathbf{y}_b(k) = \mathbf{\Phi}_{ab} \mathbf{x}_b(k). \tag{21c}$$

For this artificial system (21) with well-known entrance vector $\boldsymbol{v}$, *Luenberger* observer can be sketched (Fig. 9).

In Table 3 the state-space main data obtained via LQR method are presented.

4. SIMULATION RESULTS

The models of AMB and digital control software had been implemented in *MATLAB/Simulink* to get simulation results. In Figs. 10, 11, 12 and 13, the calculated position and current variations during rotor lifting are presented.

The main difference between Figs. 10 and 11 is the absence of overshoot in the rotor movement with state-space controller, compared to the PID controller, with almost identical lift-off time needed to reach the zero reference position. The oscillations in the rotor movement with the PID controller are also reflected by the behavior of its control current in Fig. 12.

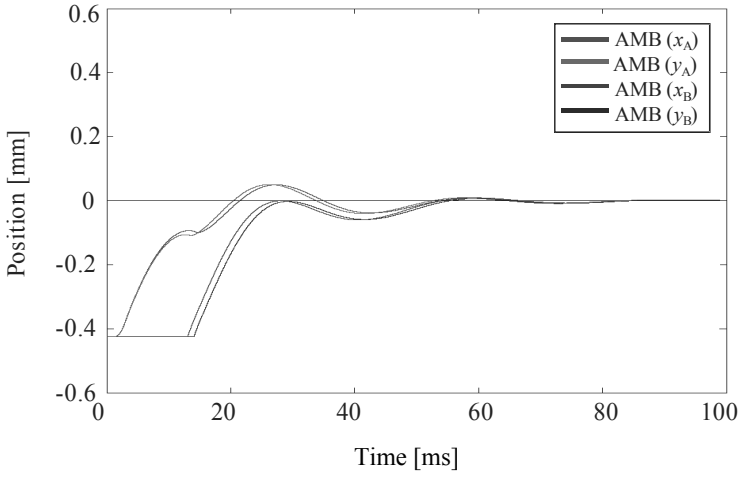

Fig. 10 – Calculated rotor positions, using PID control of radial AMB of all four axes *x, y* for A and B-bearing.

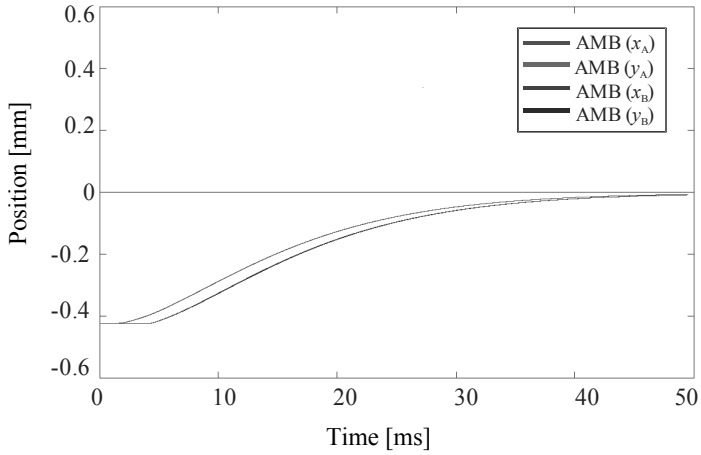

Fig. 11 – Calculated rotor positions, using State Space Control of radial AMB of all four axes *x, y* for A- and B-bearing.

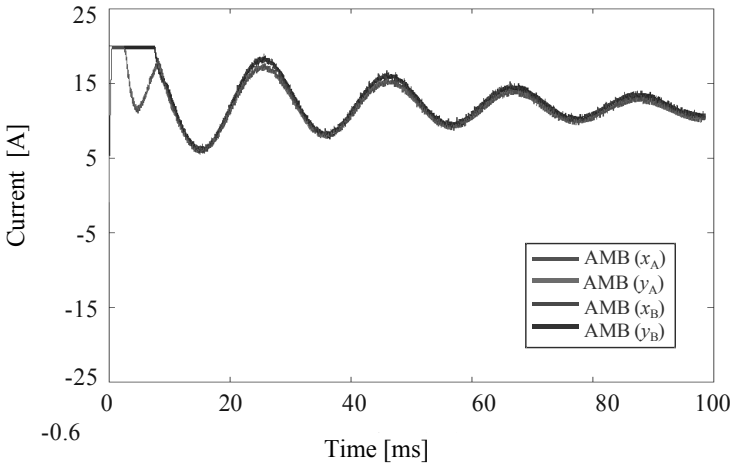

Fig. 12 – Calculated currents i_c , required for rotor lifting with PID control.

Although both controllers manage to bring the system in steady state, it is very important to maintain the rotor in levitation, when a disturbance acts upon the system. In order to study the behavior of both control methods, two types of disturbances will be considered:

1. Static disturbance simulated as a force step (*step function model*) is applied to rotor at 17 s after system is started. The static disturbance force $\boldsymbol{f}_d$ equals 100 N.

The force is located at the axial outer side of the rotor near bearing B with a distance of 231 mm from the gravity center O. Angle between the direction of gravitation force and disturbance force is –30°.

2. Imbalance effect due to rotor center of gravity dislocation from rotational axis by a certain displacement e_s. Dislocation e_s of gravity center O from rotational axis (that is centered at rotor geometrical center) is given by an additional mass Δm_s on the rotor surface at each axial position of magnetic bearings.

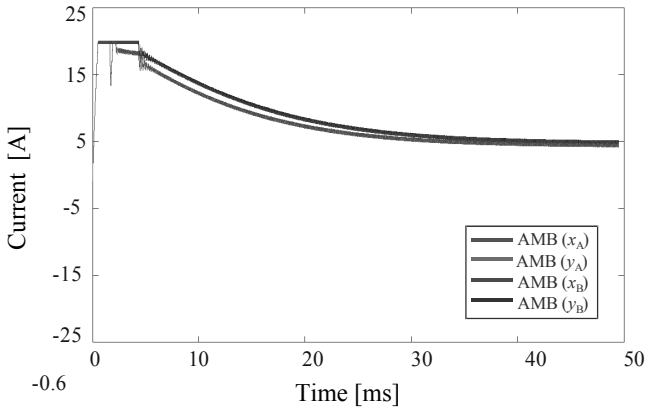

Fig. 13 – Calculated currents i_c , required for rotor lifting with state-space control.

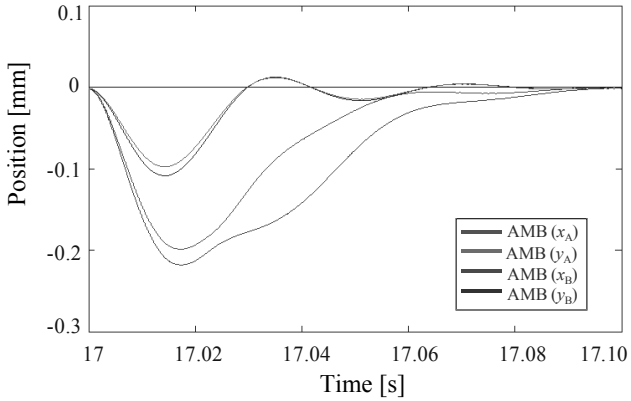

Fig. 14 – Calculated PID rejection of a static disturbance at speed 40 000 rot/min.

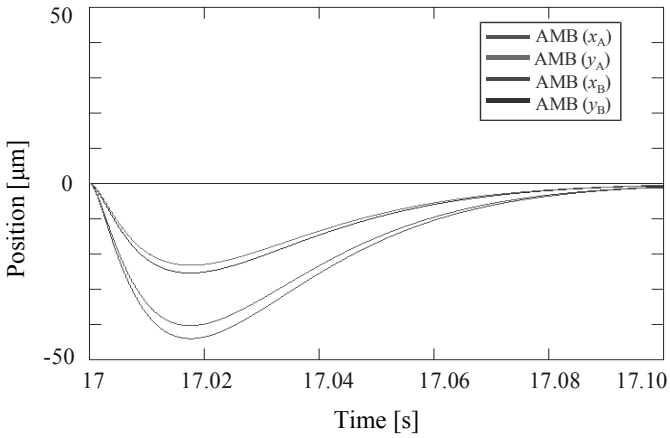

Fig. 15 – Calculated state-space rejection of a static disturbance at speed 40 000 rot/min.

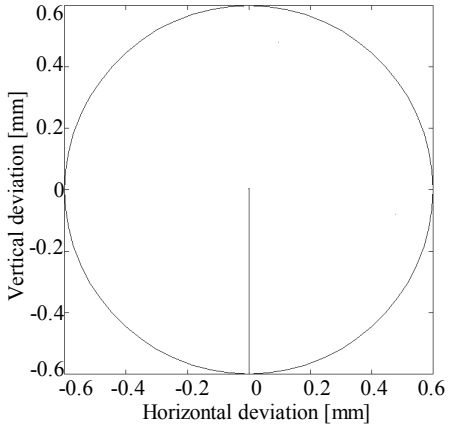

Fig. 16 – Calculated rotor orbit of state-space control with static imbalance from lift-off to rotational speed at 40 000 rot/min.

In Figs. 14 and 15, the simulation results are presented, which were obtained for static disturbance force that appears when rotor is rotating. We can see, that the state-space controller can maintain the rotor position better than the PID controller (displacement of the rotor up to 200 μm with the PID controller, against the rotor displacement up to 50 μm with the state-space controller).

In Fig. 16, the geometric locus of symmetry axis of bearing B with state-space controller is shown during the rotor movement from lifting-off at standstill and acceleration up to 40 000 rot/min, when the rotor imbalance is applied according to ISO 1940 (Q = 2.5 mm/s at 40 000 rot/min). This corresponds with two masses, each Δm_s of 94 mg, fixed on the rotor surface. Each mass is placed at each magnetic bearing axial distance from the rotor gravity center. The resulting periodical force due to the imbalance equals 74.2 N for the total rotor. The movement in detail is shown in Fig. 17, where the rotor is oscillating in a small range of 0.6 μm around the zero reference position.

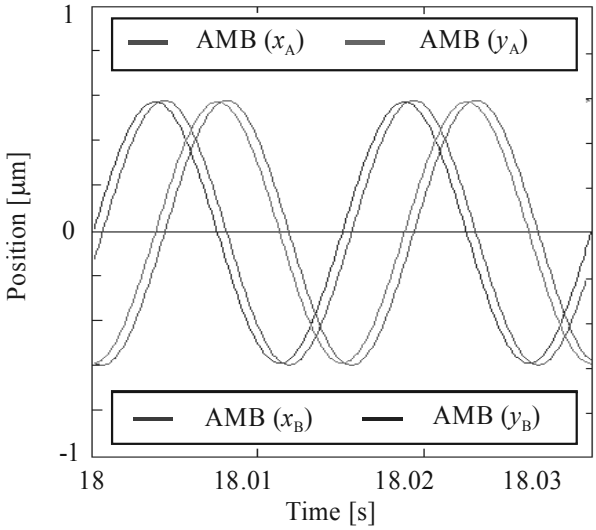

Fig. 17 – Zoomed calculated position behavior of Fig. 16.

5. **EXPERIMENT RESULTS**

The control algorithm is implemented on a DSP platform TMS320F2812, which is used in a test-bench (Fig. 18). The implementation data of the AMB is listed in Table 4.

In experiments at our test bench, the performance of the active magnetic bearings, controlled by a digital PID controller, were investigated. The rotor positions were measured during the turn-on of the active magnetic bearing and during an external step disturbance force of 40 N.

Table 4

Specification of the active magnetic bearing system

DSP TMS320F2812:	
Clock frequency	150 MHz
A/D-converters	12 bits
Internal PWM generators	12 modules
PID Control Algorithm:	
Position controller rate	9.375 kHz
Current controller rate	93.75 kHz
Power Amplifier:	
Rated current	20 A
Rated voltage	24 V
Position Sensor	
Type	Eddy-Current

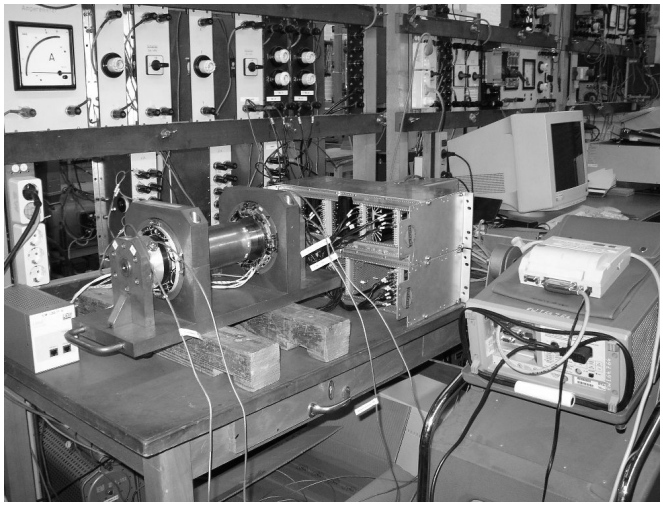

Fig. 18 – Magnetic bearing test-bench at *Darmstadt University of Technology*.

Figure 19 shows the locus of the A- and B-side of the rotor during the turn-on of the active magnetic bearing system. The zero position represents the middle point of the stator-fixed frame. The negative part of the axis y_A and y_B have the same direction as the gravitation force. Before the turn-on, the rotor was lying on the auxiliary bearings, which have an air gap of 200 μm. Therefore the initial rotor positions at both A- and B-side are located at $y_A = y_B = -200$ μm. During the turn-on, the rotor position has an overshoot up to approximately $y_A = 50$ μm, and reaches at the steady-state the zero position. The overshoot is typical behavior due to the strong proportional gain K_P of the PID controller.

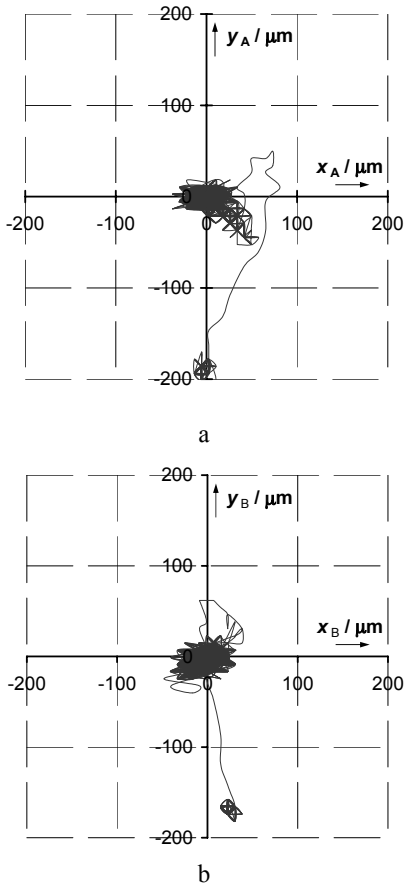

Fig. 19 – Measured rotor position locus during the turn-on of the magnetic bearing with digital PID controller at the: a) A-side; b) B-side;
(K_P = 50516.57 A/m, K_D = 89.81 As/m, K_I = 52631.58 s^{-1}A/m).

The comparison of measurement and calculation is shown in Fig. 20 for the rotor position in the axis y_A during the turn-on of the magnetic bearing. The simulation model of the active magnetic bearing system in MATLAB/Simulink was linearized at the operating point in the zero position. The real active magnetic bearing generates forces, which have quadratic dependency from the winding current and the rotor displacement. This is the reason of the differences between the calculated and measured rotor positions.

The measured rotor position in Fig. 20a shows that the rotor at about $t = 0.5$ s jumps to a position $y_A \approx -40$ µm, while the calculated rotor position shows the

rotor moving to $y_A \approx 0$ directly, apart from oscillations in the calculated rotor position for about 75 ms into the steady state position $y_A = 0$ at $t \approx 575$ ms (Fig. 20c). In reality (measured rotor position), there is always slight asymmetry on the rotor position inside the air gap, therefore the rotor does not move directly into the zero position. This is compensated by the integrative part K_I of the PID-controller, visible on the rotor movement at 0.5 s $\leq t \leq$ 2 s (Fig. 20b). For $t > 2$ s, the measured rotor position has reached the zero position.

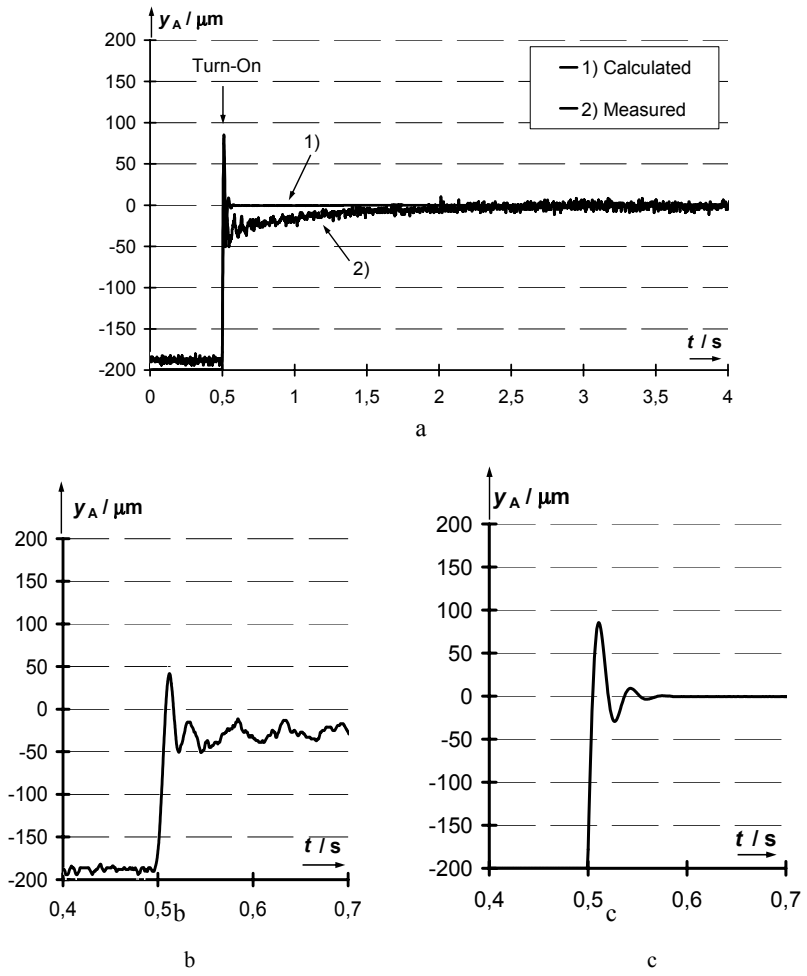

Fig. 20 – Rotor position of the axis y_A during turn-on at $t = 0.5$ s of the magnetic bearing: a) comparison of calculated and measured position; b) measured position; c) calculated position ($K_P = 50516.57$ A/m, $K_D = 89.81$ As/m, $K_I = 52631.58$ s^{-1}A/m).

Figures 21–23 show the rotor position locus during a step disturbance of 40 N at standstill ($n = 0$). The step disturbance in the measurement was realized by a falling iron block with a mass of 4.075 kg and a falling distance of 2 cm. Comparison between Fig. 21 and Fig. 22 show the influence of different proportional part K_P of the PID-controller. With higher K_P, the active magnetic bearing system has higher stiffness, resulting in a lower maximum displacement of the rotor. This displacement is $y_A \approx -100$ μm at Fig. 21, which has 1.5 times higher K_P compared to Fig. 22. There, the displacement is $y_A \approx -200$ μm.

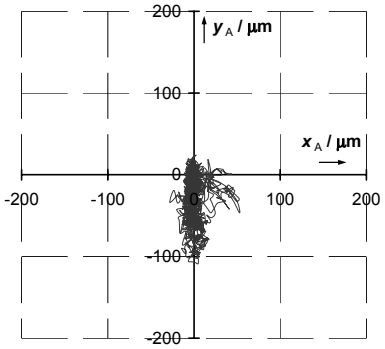

Fig. 21 – Measured rotor position locus at the shaft A-side during a step disturbance of 40 N on the middle of the shaft at standstill ($n = 0$, $K_P = 50516.57$ A/m, $K_D = 89.81$ As/m).

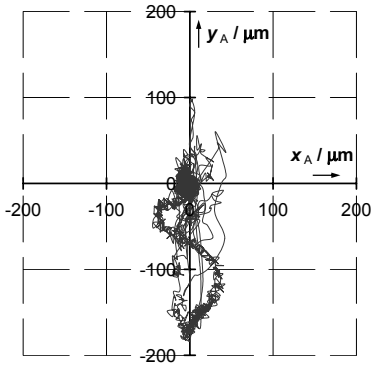

Fig. 22 – Measured rotor position locus at the shaft A-side during a step disturbance of 40 N on the middle of the shaft at standstill ($n = 0$, $K_P = 33677.71$ A/m and $K_D = 89.81$ As/m).

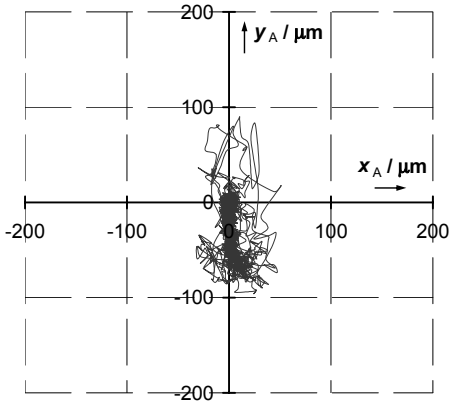

Fig. 23 – Measured rotor position locus at the shaft A-side during a step disturbance of 40 N on the middle of the shaft at standstill ($n = 0$, $K_P = 50516.57$ A/m and $K_D = 59.87$ As/m).

Compensating fast dynamic disturbance depends on the derivative part K_D of the PID controller. This is shown by the comparison of the measured rotor positions between Fig. 21 (K_D = 98.81 As/m) and Fig. 23 (K_D = 59.87 As/m). Higher value of K_D keeps the rotor position deviation dynamically in a smaller range.

Several influences limit the maximum value of K_D. It must be kept in mind that too high K_D value can amplify coupled undesired signal noise resulting in oscillations of the controller output that can disturb the controller performance. Therefore, in the digital controller a digital finite impulse response filter (FIR filter) is applied together with analogue low-pass filter to minimize the signal noise coupled into the controller loop.

Furthermore, the power amplifier has a current limit of 20 A (Table 4). With stronger dynamic disturbance and thus higher derivative gain output, the power amplifier will reach its current limit. Thus, no additional compensation of the dynamic disturbance can be performed.

Corresponding to the locus in Fig. 21, Fig. 24 shows the time functions of the rotor positions in the axis y_a during the step disturbance. The iron block fell onto the rotor shaft in gravitation force direction at given times marked by the text "40 N load" at its beginning, which yields the step disturbance statically. However, the first impact of the iron block on the rotor shaft results in a dynamic disturbance which can not be assumed as a pure step disturbance. In the calculation result, a pure step disturbance with 40 N was used. This is one reason for the measured rotor position oscillations at the beginning of the disturbance. In Fig. 24, the calculated and measured rotor positions are compared to each other. Statically, the results of the calculation and measured rotor positions have similar behavior.

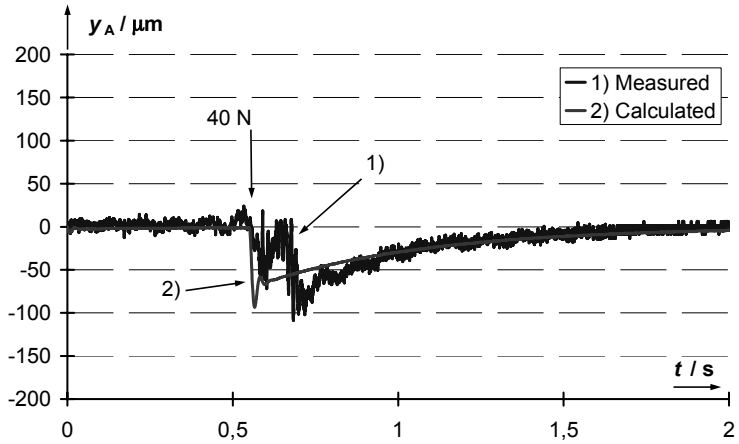

Fig. 24 – Comparison of calculated and measured rotor position of axis y_a due to step disturbance of 40 N on the middle of the shaft at standstill (n = 0, K_P = 50516.57 A/m, K_D = 89.81 As/m, K_I = 52631.58 s^{-1}A/m).

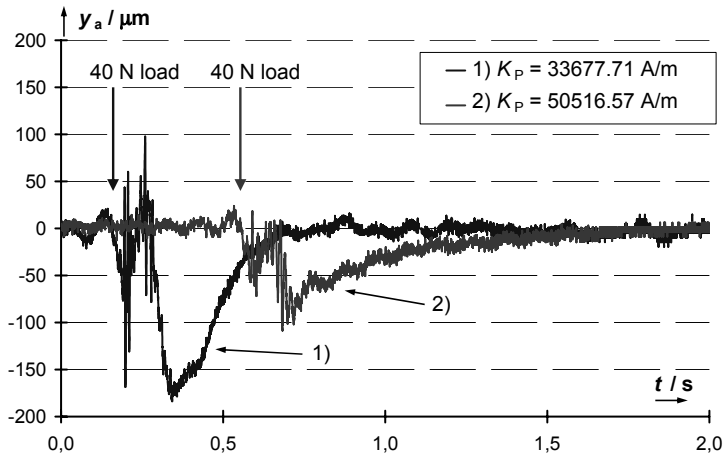

Fig. 25 – Measured rotor position of the axis y_a during a step disturbance of 40 N on the middle of the shaft at standstill ($n = 0$) with different K_P.

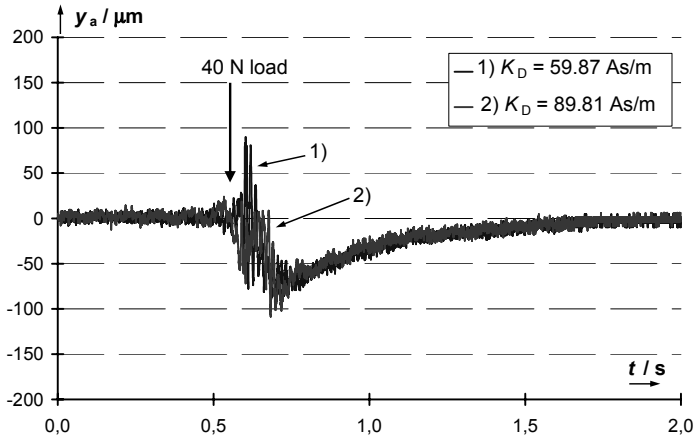

Fig. 26 – Measured rotor position of the axis y_a during a step disturbance of 40 N on the middle of the shaft at standstill ($n = 0$) with different K_D.

Corresponding to the comparison of different K_P in Fig. 21 and Fig. 22, the time functions of the measured rotor positions are shown in Fig. 25. Fig. 26 shows the measured rotor positions with different derivative gain K_D of the PID-controller, as already discussed in the comparison of Figs. 21 and 23.

6. **CONCLUSIONS**

The advantages of state-space control method in the magnetic bearings compared to digital PID control are presented by simulation. The time required for reaching standstill position in state-space control is shorter by about 9% than in PID case and the rotor moves to the reference position without any oscillations.

The simulations were demonstrated by taking into consideration the load disturbances on the rotor shaft. Experiments on the digital PID controller were performed to verify the simulated PID behavior. Implementation of the state-space controller on the experimental set-up is currently under process.

Although state-space method is offering better control performance, it must be said that the implementation of the software on a DSP and the DSP system requirements, like necessary software space of control algorithm implementation and allowable sensor signal noise at the DSP inputs, are more complex than in the PID case.

Received on 16 July 2006

REFERENCES

1. M. Klohr, A. Binder, J. Eichhorn, *Bemessung und Simulation eines magnetgelagerten Permanentmagnet-antriebs (MAGPERM) 40 kW, 40.000 min^{-1}*, 4. Workshop Magnetlagertechnik Kassel – Zittau, Kassel, 1999, pp. 18–24.
2. G. Schweitzer, A. Traxler, H. Bleuler, *Magnetlager – Grundlagen, Eigenschaften und Anwendungen berührungsfreier, elektromagnetischer Lager*, Berlin, Springer Verlag, 1993.
3. G.F. Franklin, J.D. Powell, M.L. Workman, *Digital Control of Dynamic Systems*, 2nd Edition, Boston, Addison-Wesley, 1990.
4. J. Adamy, *Systemdynamik und Regelungstechnik*, Vol. I, Herzogenrath, Shaker-Verlag, 2001.
5. M. Klohr, Ch. Hinkelmann, A. Binder, *State Space Control of a High Speed Rotor on Active Magnetic Bearings*, International Symposium on Electromagnetic Fields in Electrical Engineering ISEF, Cracow Poland, 2001, pp. 593–598.
6. P. Wurmsdobler, H. Jörgl, H. Springer, *State Space Adaptive Control for a Rigid Rotor Suspended in Active Magnetic Bearings*, Proceedings of the 5th International Symposium on Magnetic Bearings, 1996, pp. 185–190.
7. R.D. Williams, F.J. Keith, P.E. Allaire, *Digital Control of Active Magnetic Bearings*, IEEE Trans. on Industrial Electronics, **37**, *1*, February 1990, pp. 19–27.
8. M. Klohr, A. Binder, T. Schneider, *Losses in High Speed Permanent Magnet Motor with Magnetic Levitation for 4 0000/min, 40 kW*, Proceedings of the 16th International Conference On Electrical Machines (ICEM), 5.-8.9.2004, Vol.1, Cracow Poland, pp. 93–94 (full version 6 pages on CD-ROM).